A Highly Integrated Ambient Light Robust Eye-Tracking Sensor for Retinal Projection AR Glasses Based on Laser Feedback Interferometry

JOHANNES MEYER, Corporate Sector Research and Advance Engineering, Robert Bosch GmbH, Germany
THOMAS SCHLEBUSCH, Corporate Sector Research and Advance Engineering, Robert Bosch GmbH, Germany
ENKELEJDA KASNECI, University of Tübingen, Germany

Robust and highly integrated eye-tracking is a key technology to improve resolution of near-eye-display technologies for augmented reality (AR) glasses such as focus-free retinal projection as it enables display enhancements like foveated rendering. Furthermore, eye-tracking sensors enables novel ways to interact with user interfaces of AR glasses, improving thus the user experience compared to other wearables. In this work, we present a novel approach to track the user's eye by scanned laser feedback interferometry sensing. The main advantages over modern video-oculography (VOG) systems are the seamless integration of the eye-tracking sensor and the excellent robustness to ambient light with significantly lower power consumption. We further present an algorithm to track the bright pupil signal captured by our sensor with a significantly lower computational effort compared to VOG systems. We evaluate a prototype to prove the high robustness against ambient light and achieve a gaze accuracy of 1.62 °, which is comparable to other state-of-the-art scanned laser eye-tracking sensors. The outstanding robustness and high integrability of the proposed sensor will pave the way for everyday eye-tracking in consumer AR glasses.

140

CCS Concepts: • **Human-centered computing → Mixed / augmented reality**; • **Hardware** → *Displays and imagers.*

Additional Key Words and Phrases: Low-power eye tracking, MEMS scanned laser eye tracking, retinal projection, AR glasses

ACM Reference Format:
Johannes Meyer, Thomas Schlebusch, and Enkelejda Kasneci. 2022. A Highly Integrated Ambient Light Robust Eye-Tracking Sensor for Retinal Projection AR Glasses Based on Laser Feedback Interferometry. *Proc. ACM Hum.-Comput. Interact.* 6, ETRA, Article 140 (May 2022), 18 pages. https://doi.org/10.1145/3530881

1 INTRODUCTION

Robust and highly integrated eye-tracking sensors are a key technology to improve resolution of display technologies like focus-free retinal projection for augmented reality (AR) glasses e.g. by enabling display enhancement methods like foveated rendering [18, 21, 22]. Furthermore eye-tracking allows to steer the exit pupil increasing the display's field of view (FOV) [15, 21] of AR glasses. In addition to display enhancement techniques, eye-tracking sensors enable novel ways

Authors' addresses: Johannes Meyer, Corporate Sector Research and Advance Engineering, Robert Bosch GmbH, Renningen, Germany, Johannes.Meyer2@de.bosch.com; Thomas Schlebusch, Corporate Sector Research and Advance Engineering, Robert Bosch GmbH, Renningen, Germany, Thomas.Schlebusch@de.bosch.com; Enkelejda Kasneci, University of Tübingen, Tübingen, Germany, Enkelejda.Kasneci@uni-tuebingen.de.

Permission to make digital or hard copies of all or part of this work for personal or classroom use is granted without fee provided that copies are not made or distributed for profit or commercial advantage and that copies bear this notice and the full citation on the first page. Copyrights for components of this work owned by others than the author(s) must be honored. Abstracting with credit is permitted. To copy otherwise, or republish, to post on servers or to redistribute to lists, requires prior specific permission and/or a fee. Request permissions from permissions@acm.org.
© 2022 Copyright held by the owner/author(s). Publication rights licensed to ACM.
2573-0142/2022/5-ART140 $15.00
https://doi.org/10.1145/3530881

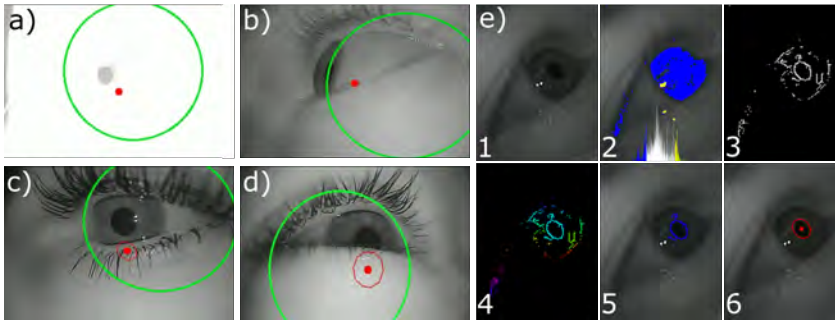

Fig. 1. Key challenges of VOG based eye-tracking sensors is a robust detection of the pupil, which is limited due to a) limited dynamic range of camera sensors to operate under a wide range of ambient illumination settings e.g. in bright sun light, b) detection of the pupil over the whole field of view due to the high off-axis integration of camera sensors, c) false pupil detection e.g. due to mascara, other disturbances, dirt on the lens and d) false detection due to partly occluded pupils by lashes or eye lids. Furthermore the pupil detection is rather computational complex as several image processing steps are required to extract the pupil as shown in e)

to seamlessly interact with the user interface of AR glasses [5, 26, 27], improving thus the user experience.

Video oculography (VOG)camera sensors are the state-of-the-art in mobile eye-tracking, tracking either the pupil in the 2D image and estimate gaze using a geometric 3D eye model [42], or track the pupil and corneal reflections from additional infrared (IR) LEDs and use a regression-based approach to determine gaze direction, as shown by [16]. In both cases, the key to robust eye tracking is robust detection and tracking of the pupil under a variety of conditions, which is, as shown in Figure 1, not always the case with current VOG systems.

A well-known issue with state-of-the-art VOG sensors is the limited dynamic range of camera sensors, leading to a loss of the pupil signal in presence of varying ambient light or in bright sun light [12, 19], as illustrated in Figure 1 a).

Furthermore the high off-axis integration of camera sensors in current VOG systems, as illustrated in Figure 1 b) [20, 45], leads to a loss of pupil detection especially if the gaze vector points away from the cameras optical axis, which allows robust eye-tracking only in a part of the user's FOV [30]. This problem is solved by adding more camera sensors to cover a larger field of view, such as proposed by [44] or [46]. However, this leads to more complex sensor integration as well as higher power consumption stem from additional sensors and higher complexity eye-tracking algorithms.

Additional cases which leads to a false pupil detection are due to the wearing of mascara [17], as false edges are considered as pupil edges by the pupil detection algorithm, illustrated in Figure 1 c). A similar case is shown in Figure 1 d) where a part of the pupil is occluded by the eyelid, which also leads to a false pupil detection [9, 12]. This issues is addressed by more advanced pupil detection algorithms e.g. by using convolutional neural networks like PupilNet [10], RITNet [2] or the Deep VOG approach by [48]. The main drawback of these advanced algorithms is increased demand of processing power which increases the power consumption of VOG eye-tracking systems.

Finally, VOG algorithms require several steps of image processing to extract pupil features from camera images, as shown in Figure 1 e), which illustrates the processing steps of the VOG algorithm proposed by [20]. There are several variants of the algorithm with optimization of individual steps of the pupil detection pipeline to improve detection accuracy and robustness, e.g. ELSE [11], PURE [34] or PUREST [35]. The increased robustness is accompanied by higher computational requirements. In recent years this issue is addressed by pupil detection algorithms which are optimized with respect to computational requirements and latency e.g. by [7] or [6].

The presented disadvantages of VOG sensors and the corresponding power consuming eye-tracking algorithms indicate that the sensing technology itself puts some hurdles for eye-tracking sensor integration into AR glasses. To enable robust eye-tracking and overcome these limitations, we introduce a low power eye-tracking sensor approach using laser feedback interferometry (LFI) sensing technology to integrate eye-tracking capability into retinal projection AR glasses.

The LFI sensor is composed of a tiny vertical cavity surface emitting laser (VCSEL), operating at the infrared (IR) regime. In addition, a photodetector is integrated into the laser cavity using semiconductor processes. The small sensor size enables high integration into the frame temple of AR glasses. Integration of the photodetector enables the LFI sensing method, a coherent sensing method, leading to a high robustness against ambient light as most light stemming not from the lasers own radiation is suppressed [28]. Thus the sensor is capable to robustly operate in presence of ambient light [25].

To solve the sensor integration problem and the high-off-axis integration of VOG systems, we further propose to integrate the LFI IR laser sensor into a retinal projection AR glasses system which consists of a micro-electro-mechanical system (MEMS) micro mirror based laser scanner and a holographic optical element (HOE) to steer the laser beam towards the eye.

Furthermore, we exploit the unique sensing modality of the LFI sensor and propose a low-power pupil detection and tracking algorithm by exploiting the characteristic bright pupil signal.

Our contribution is three fold:

(i) We propose an highly integrated eye-tracking sensor approach for retinal projection AR glasses based on an ambient light robust LFI sensor. By combining the LFI sensor with a highly transparent IR HOE and a MEMS micro mirror we further solve the highly-off-axis sensor integration. In addition, the eye tracker is invisible to the user, as it is fully integrated into the frame temple.

(ii) We propose an algorithm optimized to detect and track the pupil based on the characteristically bright pupil signal captured by the LFI sensor and

(iii) We evaluate the resulting gaze accuracy of the proposed algorithm and the ambient light robustness of the proposed sensor experimentally in a prototype setup.

Compared to the work of [24] we switch from an IR laser with external photodiode to the LFI sensor with integrated photodiode and further show the high integratability into a glasses frame. In addition we manufacture the high transparent IR HOE, which is mandatory for the system.

Compared to the work of [25] we apply the LFI sensor to human eyes and proof the proposed bright pupil effect. We further evaluate gaze accuracy in a human study with 20 participants and further propose an power saving algorithm for pupil detection algorithm.

In the upcoming Section the state-of-the-art w.r.t. scanned IR laser eye-tracking sensors is discussed. Afterwards, in Section 3, we introduce the proposed eye-tracking sensor and describe briefly the system components. Furthermore, we describe the underlying sensing principle of the LFI sensor technology as well as the origin of the observed bright pupil pattern. In addition, we describe our algorithm to detect and track the pupil. In Section 4, we describe our setup used to evaluate the gaze accuracy and compare it to a VOG system. Further, we show the robustness against artificial light. Finally, we compare our results with other state-of-the-art scanned IR laser eye-tracking approaches, discuss the applicability for AR glasses w.r.t. power consumption, sensor integration, glasses slippage and system latency, and finally draw a conclusion from our work.

2 RELATED WORK

One of the first works which address scanned IR laser eye-tracking technology for AR glasses was introduced by [38]. The authors used a 2D MEMS mirror to scan the beam of an laser operating in the IR regime in a 2D pattern over the eye's surface. The photodiode, which receives backscattered light, was integrated close to the nosepad while the scan unit consisting of the IR laser and the 2D MEMS mirror were integrated into the glasses frame temple. The photodiode detects corneal reflections originating from the eye's surface [37]. To obtain the horizontal gaze angle, the MEMS mirror scan angle under which a corneal reflection was detected by the photodiode is captured. To further obtain the vertical gaze angle [37] proposed a hill climbing algorithm using the the photodiode amplitude variation as feature. To address ambient light robustness, an optical bandpass filter was applied to the front of the photodiode. The authors reported a gaze resolution of $\approx 1^\circ$ with an update rate of 3300 Hz while their system consumes less than 15 mW power.

A major drawback of their method is the vulnerability to glasses slippage. As gaze angles are directly linked to the MEMS mirror scan angles via calibration, the system requires calibration after occurrence of slippage of the glasses [37].

To achieve slippage robustness, the authors most recently released MindLink [29], which incorporates five photodiodes attached around the spectacle frame and a 2D MEMS micro mirror placed in the nose pad of the glasses. With this improved setup, the authors reported a gaze accuracy of $<1^\circ$ over a FOV of 40° x 25° and achieved an update rate of 500 Hz.

[24] approach slippage robustness by scanning an IR laser beam with a 2D scan path over the surface of the eye. The scan path was formed using two 1D MEMS mirrors for vertical and horizontal deflection. Backscattered light from the eye is measured by a photodiode, which is placed in the frame temple. The measured intensity variation over both the horizontal and the vertical scan angles is used to construct a gray scale image of the eye's surface. By applying a state-of-the-art VOG algorithm [8], they achieved a gaze accuracy of 1.31° with an 60 Hz update rate. The authors further reported a power consumption of 11 mW and estimated a theoretical resolution of 0.28° with an improved optical design. To increase robustness against ambient light they propose to use optical filters in front of their photodiode circuitry, similar to [37].

Most recently, EyeWay Vision [15] released a scanned IR laser based eye-tracking sensor to steer the exit pupil for their retinal projection AR glasses. In a previous evaluation of the prototype system by [17] a gaze accuracy of 1.72° at a sampling rate of the corneal reflection signals of 4000 Hz was reported. For absolute eye-tracking accuracy and to compensate translation movements of the eye with respect to the glasses e.g. due to slippage, a stereo camera with a sample rate of 120 Hz was added to the laboratory setup.

All above-mentioned related approaches used a photodiode to capture back reflected light of an IR laser, which was scanned in a 2D pattern over the surface of the eye. Sarkar et. al.[29, 37] and EyeWay Vision [17] focus on glint features from the cornea, the limbus or the retina to estimate the gaze direction while [24] reconstruct a gray scale image and extract the dark pupil from the image by applying state-of-the-art VOG algorithms.

All methods have drawbacks with respect to ambient light robustness, which are addressed by protecting the photodiode with optical filters from ambient light. Furthermore, the glint feature based approaches by Sarkar et. al. and EyeWay Vision tend to have issues with slippage. To address this issue they either add an reference sensors or additional photodiodes, which adds to the overall power budget of these systems. Furthermore the approaches of [24] and [17] are validated only in a laboratory setup and the sensor integration is not fully solved.

In our approach, we address the issue of ambient light robustness and sensor integration by using the LFI sensor technology. We further follow the path of [24] and use a 2D scan pattern to reconstruct gray scale images to extract the bright pupil feature. With this approach, we address the issue of a high power consumption by exploiting the bright pupil effect to directly detect the pupil in an image to reduce computational complexity.

3 SCANNED LASER FEEDBACK INTERFEROMETRY

Figure 2 illustrates the integration of the LFI sensor into the retinal projection AR glasses to form a scanned LFI eye-tracking sensor. The LFI sensor component is added to the RGB module, integrated

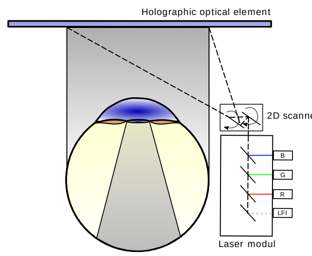

Fig. 2. The LFI sensor added to the RGB module and shares the same optical path as the visible light. The holographic optical element acts as a wavelength selective mirror and redirects the scanned laser pattern to the eye's surface.

in the glasses frame temple. The IR laser of the VCSEL is coupled via a prism into the beam path of the visible light of the RGB lasers and the combined beam is scanned via a MEMS mirror module over the HOE surface. The HOE acts as a wavelength selective mirror which parallelised the incoming beam pattern and redirects it towards the eye region.

The HOE is recorded into a photopolymer (Bayfol HX TP photopolymer) by constructing a reference wavefront and an imaging wavefront and expose the photopolymer with both wavefronts. As our photopolymer is only active for visible light, we recorded the HOE at a wavelength of 650 nm with an angular offset such that if the HOE is played back at 850 nm under an different angle the desired wavefront is reconstructed. [47] and [49] gave a detailed description of the recording HOEs using photopolymer with an angular offset.

The MEMS mirror module contains two 1D MEMS mirrors to scan in a 2D pattern over the HOE. The horizontal mirror scans in a sinusoidal pattern, while the vertical MEMS mirror is non resonantly actuated using an electrodynamic driver to steer the sinusoidal pattern vertically over the HOE. With the known geometry and the mirror deflection angles $\alpha_h(t)$ and $\beta_v(t)$, the corresponding intersection point of the laser beam with the HOE can be calculated. For a detailed description of the geometry and the image generation we refer to [24]. The scan pattern is illustrated in Figure 3. HOEs are characterized by a high wavelength selectivity and optical transparency

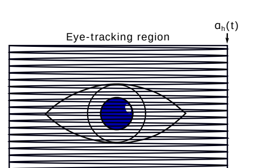

Fig. 3. Scan pattern of the laser beam over the eye's surface.

allowing integrating them invisible to the user into the glasses lenses [47].

3.1 Laser feedback interferometry

The key element in our scanned eye-tracking approach is the LFI sensor. LFI is a widely applied interferometry sensing method [43], which is used e.g. to measure displacement or velocity of solid targets. Recently, LFI sensors have also been applied to AR glasses e.g. for gaze gesture recognition [26, 27] and human activity recognition [23]. This works address the applicability of static LFI sensors for a near-eye setting.

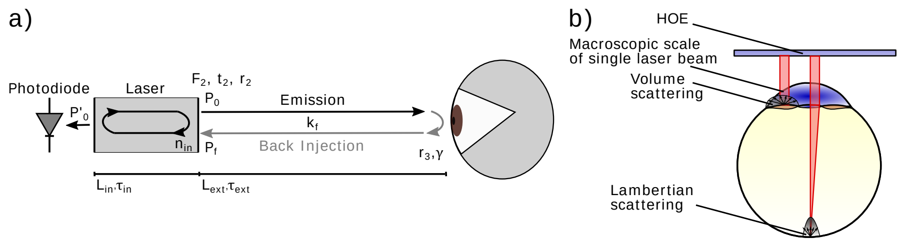

Fig. 4. a) LFI sensing scheme modeled by the well known Coupled-cavity model. Emitted light from the laser is backscattered from the eye's surface and backinjected into the cavity. The photodiode integrated into the back mirror monitors the optical power inside the cavity, which changes based on variation of the feedback path [26, 27]. b) Macroscopic scale of the laser beam hitting the outer surface (sclera, iris) of the laser or the retina of the eye.

To describe the basic sensing method of LFI sensors, the coupled-cavity model as shown in Figure 4 a) is used. The laser with its cavity length L_{int} and laser round trip time τ_{int} emits coherent light with an optical power P_0 towards the eye's surface. The laser hits the eye ball with an incident angle γ and dependent on the reflectivity and absorption, summarized by r_3, and the scattering behavior of the tissue, a fraction of the emitted power P_f is backinjected in the cavity of the laser. τ_{ext} describes the round-trip time of the laser to cross the distance L_{ext}. τ_{ext} is given by the speed of light c_0 and the refractive index n_{ext} inside the external cavity [43].

The backinjected wave interferes inside the cavity with the locally oscillating wave, which results in a optical power modulation of the laser

$$P'_0 = P_0 \left(1 + m \cdot \cos\left(\phi_{fb}\right)\right). \tag{1}$$

The feedback power P'_0 relies on the laser's optical power P_0, the modulation depth m and variations of the feedback phase ϕ_{fb}. The photodiode inside the Bragg reflector measures a tiny fraction of the optical modulated feedback power P'_0 [43].

While scanning the surface of the eye region, two effects influence the modulated feedback power P'_0. The first effect is an amplitude modulation due to varying reflectivity r_3 and scattering behavior of the different parts of the eye, which influence the modulation depth m. According to [3] m is given in a second order approximation by

$$m = 2 \cdot k_f \cdot \tau_p \cdot \left(\frac{\eta_i}{\eta_d} - 1\right) + k_f \cdot \tau_{int} \cdot (1 - F_2) \left(\frac{1 + r_2^2}{t_2^2}\right). \tag{2}$$

The feedback rate k_f describes the normalized reflected field injection rate, τ_p the photon lifetime and the fraction of η_i and η_d the differential efficiency between pump efficiency and quantum efficiency of the cavity. F_2 describes the fraction of total power which is coupled out of the front mirror of the laser cavity. The mirror is further described by its transmitivity t_2 and r_2. The feedback rate can be rewritten with respect to the three-mirror model by

$$k_f = \frac{t_2^2 \sqrt{\frac{P_0}{P_f}}}{r_2} / \tau_{int} \qquad with \qquad \sqrt{\frac{P_0}{P_f}} \propto \sqrt{\frac{r_3}{r_2}}. \tag{3}$$

Considering a constant transmitivity t_2 and reflectivity r_2 of the front mirror and a constant output of laser power P_0, the coupling factor is mainly affected by a variation of the power of backscattered light P_f due to an increase of reflectivity r_3 of the target and scattering behavior as shown in Figure 4 b).

Figure 4 b) shows the macroscopic scale of a single laser beam reflected by the HOE for two deflection angles of the micro mirror. The left beam position describes the beam hitting the outer tissue of the eye (sclera, iris) where volume scattering effects dominate the overall scattering and thus a rather low portion of light is backinjected into the laser cavity. The right beam position describes the beam hitting the retina. In this case the lens of the eye focuses the laser beam onto the retina and as the retina surface is dominated by Lambertian scattering [4], a large portion of light is back scattered. This effect is also referred as red eye effect or bright pupil effect, which is varying in severity across different human eyes [31].

The second effect which influences the modulated feedback power P_0' is given by the modulation of the feedback phase ϕ_{fb} due to speckling effects. Speckling describes the additive superposition of several backscattered signal components with random amplitude and phase. The sum of this components leads to a random modulation of the phase ϕ_{fb} of the back injected light and in particular whether constructive or destructive interference dominates the signal [13]. With respect to the eye this effect is well known from optical coherence tomography (OCT) imaging, where the signal from the retina is characterized by dark an bright speckle patterns [39].

3.2 Bright pupil detection

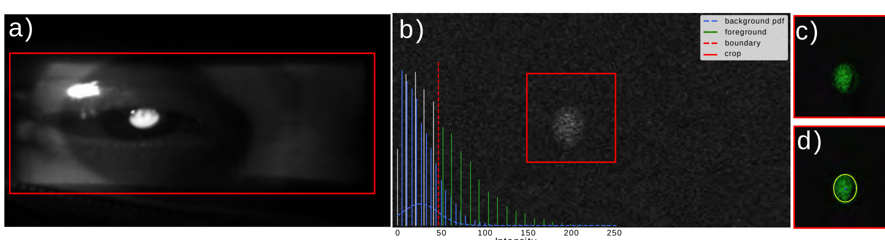

Fig. 5. a) Image of the scan area (bright area inside red box) on a person's eye taken with an IR camera looking directly through the HOE from the outside. b) Background: Modulated feedback power P_0' measured by the integrated photodiode of the LFI sensor over the scan area. Foreground: Histogram of the retinal area pixel intensity distribution (green and grey) and the non-retinal area distribution (blue). c) Segmented bright retinal area pupil pixels from b) using the intensity boundary (red dashed line). d) Multivariate Gaussian fit of the retinal area pixels in c) with pupil center in blue and pupil contour in yellow.

Figure 5 a) shows the region of the eye, scanned by the LFI sensor. An IR camera looking directly through the HOE from the outside towards the eye. The pupil appears bright when the IR laser beam hits the retina during the 2D scan, also known as the bright pupil effect. This supports our assumption that the reflectivity r_3 as well as the scattering behavior changes and therefore changes the coupling factor k_f in presence of the retina, resulting in amplitude modulation according to Equation (2). In particular, by integrating the photodiode into the back reflector of the laser cavity, IR illumination and sensing element are perfectly aligned on axis to support the bright pupil effect. In addition, the effect of speckling is clearly visible, leading to a normal distributed pattern of bright and dark speckles.

To detect the location of the pupil and therefore track the eye for each full 2D scan the following three steps are applied to each recording.

Image reconstruction: The photodiode signal of the LFI sensor is sampled in equidistant time steps t to capture the modulated feedback power $P_0'(t)$, while the MEMS mirror scans the laser beam over the surface of the eye. To generate an image of the eye region, the modulated feedback power $P_0'(t)$ and the mirror deflection angles $\alpha_h(t)$ and $\beta_v(t)$ are sampled in the same equidistant time steps. A series of samples $(P_0'(t), \alpha_h(t), \beta_v(t))$ are used to construct an image using the mirror deflection angles as pixel coordinates ($I_x \approx \alpha_h, I_y \approx \beta_v$) on the HOE and the modulated feedback power P_0' as intensity value ($I(x, y) = P_0'$) of the pixel. In Figure 5 b) in the background, a reconstructed image is shown. The pupil appears in the center of the image as a bright pattern, marked by the red box.

Pupil segmentation: Similar to VOG-based eye-tracking sensors, segmentation of the pupil is required to determine the pupil contour and center. To separate the retinal area pixels from the non-retinal area pixels of the image, a histogram-based approach is used. In Figure 5 b) the normalized histogram of the image is shown in gray and green, containing information about both the retinal area and the non-retinal area. This histogram is overlaid by a second normalized histogram (in blue), which includes only the first ten lines of the image and represents the non-retinal area area probability density distribution (PDF) $\mathcal{N}_b\left(\mu_b, \sigma_b\right)$, since there is no pupil in the first ten lines of the image. To extract the retinal area and thus separate the pupil from the non-retinal area , the intensity limit I_b (red dashed line in Figure 5 b)) is calculated by $I_b = \mu_b + \sigma_b$ based on the non-retinal area PDF. Using this limit, the normalized histogram of the image is divided into non-retinal area intensity values (gray) and retinal area intensity values (green).

Figure 5 c) shows a cropped area around the bright pupil pattern for illustration. The remaining retinal area pixels are highlighted in green.

Pupil ellipse fitting: The segmented bright pupil pattern is given as a set of p_i tuples, containing the pixel coordinates as well as the pixel intensity $p_i = (x_i, y_i, P_{0i}')$. To obtain the pupil ellipse from this set of tuples, a multivariate Gaussian distribution $\mathcal{N}_p\left(\mu_p, \Sigma_p\right)$ is fitted using least squares optimization. μ_p hereby represents the pupil center and the main components of the covariance matrix Σ_p represent the horizontal and vertical axis of the ellipse representing the pupil contour. In Figure 5 d), the resulting ellipse contour is annotated in yellow as well as the center of the ellipse as a blue dot. A pupil ellipse is therefore given by $\mathcal{E}_i = \left(\mu_{p0}, \mu_{p1}, 3 \cdot \Sigma_{p00}, 3 \cdot \Sigma_{p11}\right)$.

4 EVALUATION

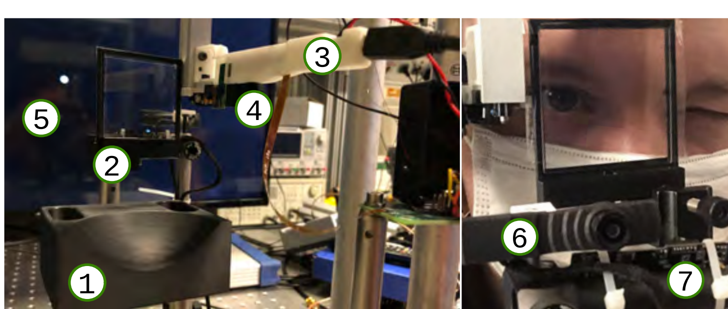

Fig. 6. Laboratory setup to evaluate the proposed scanned LFI eye-tracking sensor. The left image shows the laboratory setup from the perspective of a participant and the right image shows a participant inside the setup.

Figure 6 shows the laboratory setup used to evaluate the scanned LFI eye-tracking sensor.The LFI sensor component itself is based on an research prototype adapted from an optical communication application where IR VCSELs with monitoring photodiodes in the back DBR are common. A detailed description of the sensor component is given by Grabherr et. al. [14].

The glasses frame temple ③ with the integrated laser module and the MEMS micro mirror module ④ is based on a modified BML500P [40], an optical microsystem developed for AR glasses. The MEMS mirrors are used to scan the IR laser across the surface of the HOE, which is integrated into a flat glasses lens ②. The high transparency of the HOE allows a participant to sit in front of the laboratory setup and look through the glasses lens towards a display ⑤ on which stimuli markers are displayed. The participant's head is fixed in front of the HOE and the glasses frame temple by a chin rest ① to minimize head movements that could lead to erroneous measurements. In addition a Pupil Core V1 [20] is added to the setup. The world camera ⑥ monitors the stimuli markers on the display and an eye camera ⑦ observes the participant's eye from a bottom-up perspective through the HOE. The mirror signals $\alpha_h(t)$ and $\beta_v(t)$ as well as the interference signal $P_0'(t)$ are captured in the setup by an oscilloscope.

The Lab setup complies according to IEC 60825-1 [1] regularization to a class 1 laser system and therefore does not pose any risks to the eye. The optical power of the IR laser beam surface was limited to an optical power of 142 μW on the eye's surface, whereas the IEC 60825-1 allows a maximum optical power of 778 μW for an 8-hour continuous emission to the retina.

The low required optical power is favorable to minimizes power consumption of our scanned LFI eye-tracking sensor. Using off-the-shelf components, the power consumption of our system is estimated roughly at 30 mW. The main components contributing to the overall systems power consumption are the transimpedance amplifier (TIA) (THS4567 10 mW), which is used to amplify the interference signal $P_0'(t)$ measured by the integrated photodiode, and the analog digital converter (ADC) (MAX19191 with 15.3 mW). The gain of the TIA was set to 940 during the experiments. With further integration, additional power reduction is expected. The estimated power consumption is comparable to reported power consumption of other scanned IR laser eye-tracking sensors. In example, [37] reported a power consumption of 15 mW for their system. A major advantage of our approach is that we reuse the existing MEMS micro mirror of the RGB projection similar to [15], and therefore, did not require an additional scanner which would increase the power consumption.

4.1 Gaze accuracy

To evaluate the performance of the scanned LFI eye-tracking sensor and prove the robustness of our approach, we conducted a study with 20 participants (4 female, 16 male, mean age 34 SD(10.83)). The participant's eye colors ranged from dark brown to blue-gray. Half of the participants required vision correction ranging from +1 dpt to -2.75 dpt. Except for participant P14 who wore contact lenses, participants did not wear vision correction during the study. None of the participants were of Asian ethnicity, so the robustness of the effect of reduced bright pupil response in Asian populations as reported by [31] was not tested. All participants gave their written consent after being informed about the nature of the study.

During the study, participants sat approximately 0.6 m away from a 36" display and positioned their head on the chin rest. To set the calibration and test marker coordinates, participants were first asked to look straight through the HOE towards the display. Then, the center marker describing the resting position of the eye at $\theta = 0$ and $\phi = 0$ was adjusted to align with straight gaze. After setting the calibration and test marker coordinates, participants were asked to follow and fixate on the stimuli markers on the monitor. In a sequence 9 reference markers (red crosses in Figure 7) and 4 test markers (cyan crosses in Figure 7) are presented for approximately 5 seconds each with three repetitions resulting in a total of 39 stimuli markers presented per participant. During the experiment, scanned LFI data and images from the Pupil Core eye camera were recorded for each marker location. For each point, the first and last second of recorded data were discarded

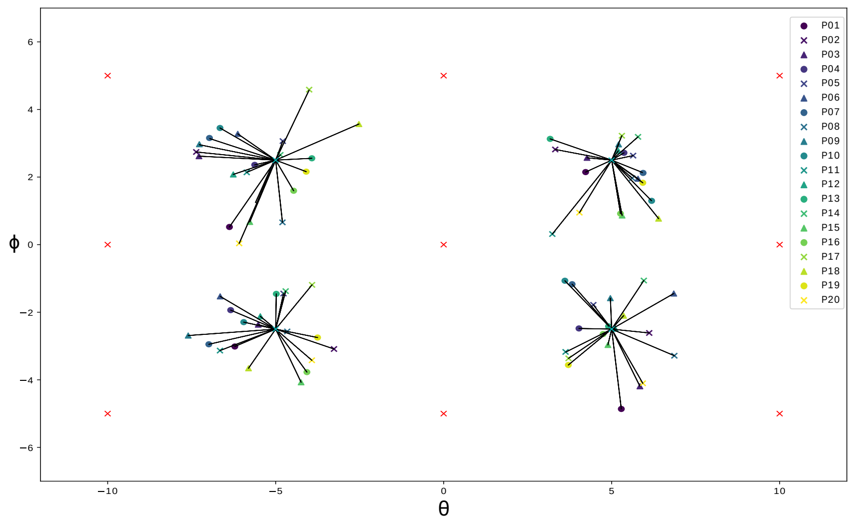

Fig. 7. Results of the gaze accuracy experiment. Participants were asked to fixate the calibration markers (red crosses) and the test markers (cyan crosses). The calculated mean gaze position per test marker and participant is added as a colored marker. In addition, an arrow shows the correlation between the calculated gaze position and the test marker.

to ensure that the participant had time to fixate on the next stimuli marker. In addition, scanned LFI sensor images were discarded if no pupil was detected due to blinking. In the Pupil Core data, detected pupil positions with a confidence < 0.8 are discarded in order to eliminate errors due to blinking as well. The pupil core camera was placed 8 cm away from the eye, which is rather large. To compensate the larger distance, the camera focus was tuned to receive sharp images at that distance. To compensate accuracy losses due to the increased distance we reduced the camera angle w.r.t. eye compared to a head worn configuration.

After data acquisition and cleaning of the raw data, the standard 9-point polynomial regression algorithm is used to map the data from pupil position space to gaze angle space. The regression algorithm was trained for each user individually and for both the scanned LFI sensor and the Pupil Core VOG sensor separately. Figure 7 shows the mapped gaze points for each participant and the 4 test points for the LFI eye-tracking sensor.

To evaluate the scanned LFI eye-tracking sensor based on the captured data, we use the accuracy as evaluation metric, which is defined as the average angular offset between estimated fixation location and the corresponding marker position. In addition, we evaluate the precision, which is defined according to [20] as the root mean squared (RMS) error between successive samples. Table 1 summarizes precision and accuracy results of the study for the scanned LFI eye-tracking sensor and the Pupil Core.

Our scanned LFI eye-tracking sensor achieves a mean gaze accuracy of 1.674°, which is comparable to the accuracy reported by other scanned laser eye-tracking approaches e.g. the 1.72° reported by [17]. The accuracy of the Pupil Core is 0.232° lower compared to our approach. In our experiments, we did not achieve the stated precision and accuracy of the Pupil Core, which is to some extent due to our laboratory setup as the scanned IR pattern appears as a varying IR illumination, which distorts the dark pupil tracking of the Pupil Core. The results of the study show that the scanned LFI eye-tracking sensor is capable to track the bright pupil with a reasonable accuracy.

Table 1. Accuracy and precision of our approach and the Pupil Core eye tracker over all participants

	Scanned LFI		Pupil Core V1	
	Precision °	**Accuracy °**	**Precision °**	**Accuracy °**
P1	1.991	2.591	0.127	1.802
P2	0.438	1.976	0.172	1.935
P3	0.718	1.239	0.644	1.597
P4	0.587	0.982	0.778	1.585
P5	1.001	1.122	0.746	0.988
P6	1.661	1.792	0.925	1.542
P7	0.512	1.408	0.830	1.820
P8	0.743	1.623	0.974	1.990
P9	1.039	2.877	0.523	1.339
P10	0.905	2.408	0.411	1.616
P11	0.455	1.888	0.830	0.820
P12	1.011	1.082	0.775	0.875
P13	0.743	1.597	0.158	0.966
P14	0.960	1.211	0.892	1.026
P15	0.569	1.077	0.058	0.847
P16	1.733	1.812	0.106	1.126
P17	1.106	1.655	0.477	1.442
P18	0.685	1.951	0.459	1.371
P19	1.138	1.750	0.291	1.181
P20	0.914	1.446	0.791	2.427
Mean	0.945	1.674	0.548	1.415
Std	0.4162	0.5052	0.3014	0.4305

4.2 Ambient light robustness

A further requirement to eye-tracking sensors for consumer AR glasses is a robust operation under variation of ambient light. To evaluate the ambient light robustness, our scanned LFI eye-tracking sensor as well as the Pupil Core VOG sensor are exposed to different illumination sources, while a participant was looking straight through the HOE such that the HOE and thus the parallel laser rays were perpendicular to the eye. Figure 8 summarizes the results of this study. The first row shows images taken with the Pupil Core V1 eye-tracking sensor using the pupil capture software (V1.17.71) with default settings while the second row shows images captured with the scanned LFI eye-tracking sensor. The last row shows a spectra of each illumination source captured by an OceanOptics4000 optical spectrometer. In addition, we measured the optical power at the wavelength of 850 nm on the eye's surface as both the the Pupil Core eye-tracking sensor and our scanned LFI eye-tracking sensor operates at 850 nm. The results are annotated in the second row of the image.

The first lighting situation we investigated was a completely dark laboratory with no external light sources. Under this condition, both sensors track the pupil as expected. The second lighting situation we investigated is office lighting. Under this very controlled lighting condition, both sensors also worked perfectly. Also under cloudy sunlight this condition, both sensors show stable operation. In bright sunlight ($P_{opt}(850\,\text{nm}) = 507\,\mu\text{W}$) the dark pupil appears only as a tiny dark spot in the camera image, which is no longer robustly detected. While the VOG camera sensor saturates, the scanned LFI eye-tracking sensor still is capable to robustly detect the bright pupil. As

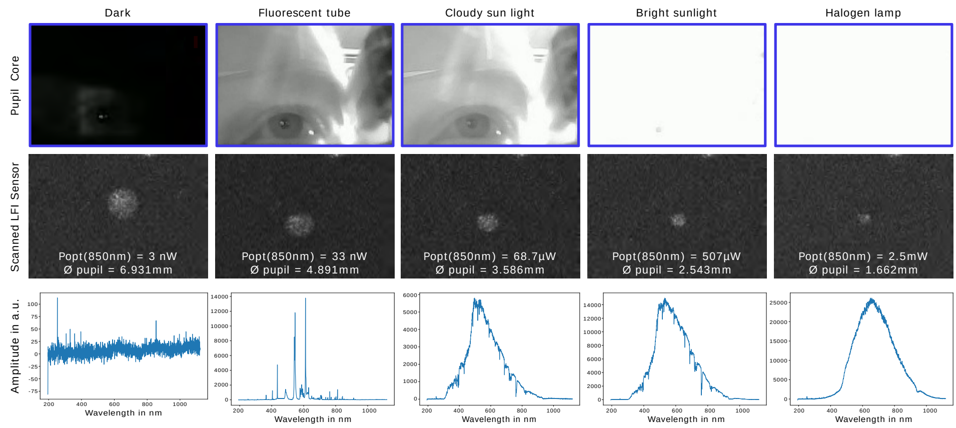

Fig. 8. Comparison of the Pupil Core V1 eye-tracking sensor and our approach with respect to ambient light robustness. The first row shows images captured by the Pupil Core. The second row shows images captured by our approach with annotated optical power of the light source at 850 nm and the estimated pupil diameter from the pupil contour. The last rows shows spectrograms of the different light sources.

already a improved version of the VOG system (Pupil Core V2) is available, which we did not used for the experiment, the image quality for the bright sun light condition might improve.

As final lightning condition, we used a halogen lamp, which is a broadband thermal radiator with characteristically high intensity in the IR wavelength region. With a measured optical power of 2.5 mW at 850 nm the eye region was exposed by a five times higher intensity compared to bright sun light. Even under this condition, the scanned LFI sensor is capable to detect the bright pupil reliably, leading to an outstanding dynamic range of the scanned LFI eye-tracking sensor. The observed high robustness to ambient light is in line with earlier work by [25].

5 DISCUSSION

To assess the quality of our scanned LFI eye-tracking approach with respect to the state of the art of scanned IR laser eye tracking approaches and discuss the results and potential limitations, we compare our approach with other scanned IR laser eye tracking approaches in Table 2.

Table 2. Comparison between different scanned IR eye tracking approaches and our approach

	[37]	[24]	[17]	**Ours**
Tracking method	Corneal reflection	Dark Pupil tracking on rasterized 2D image	Corneal reflection & Stereo image	Bright Pupil tracking on rasterized 2D image
IR Scanner	2D MEMS mirror	2x 1D MEMS mirrors	2D MEMS mirror	2x 1D MEMS mirrors
Accuracy	>1°	1.31°	1.72°	1.67°
Precision	-	0.01°	0.0091°	0.945°
Diag. FOV	35.35°	44.72°	16.97°	22.36°
Power	15 mW	11mW	-	30mW
Sample rate	3300 Hz	60 Hz	4000 Hz	60 Hz

The works of Sarkar et. al. and Holmqvist et. al. differ from the work of Meyer et. al. and our approach mainly with regard to the chosen tracking method. They track corneal reflections with a rather high sampling rate while the work of Meyer et. al. and our work rely on a rasterized 2D image and tracking of either a dark or a bright pupil. All approaches are in the same range of absolute gaze accuracy and power consumption. Furthermore, they are evaluated on a comparable diagonal FOV. The main improvements in our work compared to the state of the art is the *robustness of pupil detection*, which is extremely important for consumer AR glasses. By using the presented LFI measurement method, the sensor is almost immune to ambient light. Due to the signal characteristics of the bright pupil and the proposed algorithm, our approach overcomes several limitations of VOG eye-tracking systems, as it is robust against eyelashes that interfere with the pupil, mascara that causes false pupil detection and eyelids that partially occlude the pupil. In addition, the sensor works independently of eye color and iris structure.

5.1 Sensor integration

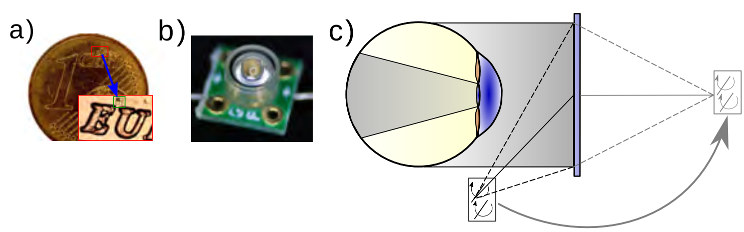

Fig. 9. Sensor integration of the scanned LFI eye-tracking sensor. a) shows a microscope image of the 160 μm x 180 μm LFI sensing element on a coin for scale (blue arrow). b) Encapsulated optical module of the research prototype composing of the LFI sensor as well as the beam shaping lens. The lens diameter is roughly 2 mm. c) virtual rotation of the MEMS scanner to the center of the FOV by the HOE to solve the off-axis integration issue of VOG sensors

In addition to robust pupil detection, our approach can be fully integrated into AR glasses with retinal projection, as the optical path of the IR laser uses the same optical path as visible light. Moreover, the VCSEL as the optical transmitter and the photodiode as the optical receiver of the LFI sensor element are highly integrated in a single chip, as shown in Figure 9 a). In combination with the beam shaping optics a diameter of the optical module of below 2 mm is possible (Figure 9 b)), allowing thus direct integration into the RGB laser module. Compared to other scanning laser approaches, such as e.g. shown by [37], our setup does not require any components to be mounted outside the spectacle temple or even in the spectacle frame. The use of an HOE allows us to virtually rotate our MEMS scanner to the front of the glasses lens as shown in Figure 9 c). Images taken with the scanned LFI eye-tracking sensor therefore appear as if taken from the perspective of a camera viewing the eye centrally from the outside through the lens. Compared to VOG systems, this effect is possible without any camera arms interfere with the users FOV. In addition, this perspective allows covering the whole eye region and it is possible to track the pupil over a large FOV.

5.2 Power consumption

[37] estimated the power consumption of VOG camera sensors at 150 mW, while our sensor consumes only about 30 mW, which is a significant improvement and allows real-time operation in lightweight consumer AR glasses. In addition, our proposed pupil detection algorithm requires less computationally intensive image processing steps to extract the pupil contour compared e.g. to the Pupil Core algorithm [20]. As the output of our pupil detection algorithm is an ellipse contour $\mathcal{E}$, the power consumption to derive an absolute gaze vector e.g. by using a geometrical 3D model approach as proposed by [41] is comparable to VOG eye-tracking systems.

5.3 Glasses slippage

A major problem that causes eye-tracking sensor accuracy to degrade is the effect of glasses slippage [32]. This issue also affects our sensor performance as we are working on image data. The impact of slippage to our sensor might however be less significantly affecting our results as the camera axis in our approach is close to the optical axis of the eye. Compared to the work of [24] we only capture the bright pupil and do not gather further any information from the eye region. Thus slippage compensation by tracking landmarks like the eye corners as introduced by [33] is not feasible. A possible solution to achieve slippage robustness for our approach is to adopt the approach of [36] to derive slippage robust features from a geometric 3D eye model, which we will consider and evaluate as part of our future research.

5.4 Update rate, latency and motion blur

Due to the tight coupling of the optical path of the RGB projection and the IR path the update rate is limited to 60 Hz, which is compared to [37] and [17] rather low.A faster scanning MEMS mirror would improve the update rate to some extend. However, since the diameter of the laser beam determines the minimum required mirror diameter, mirror miniaturization is limited, resulting in a maximum technically feasible scan frequency of 120 Hz. Compared to VOG systems latency is rather low as in our approach we capture images pixel by pixel, and therefore, the foreground background segmentation can be performed in parallel to image capturing, leading to a latency of 0.0166 s to calculate the pupil ellipse $\mathcal{E}$. A camera sensor captures all pixels in parallel while in contrast our system captures images sequential. Thus a fast saccadic movements of the pupil during image acquisition can lead to elliptical distortions of the captured ellipse $\mathcal{E}$.

5.5 Gaze angle dependency of bright pupil effect

The bright pupil effect appears only if both the illumination axis and the sensor axis are close to each other. The scanned LFI system moves both the light source and the detector in parallel, leading to a perfect alignment of both axes. However, a disadvantage of our system is the collimated nature of the laser beam compared to a diverging IR light source. If the laser beam is not approximately perpendicular to the retina due to the Lambertian scattering less light is back injected into the laser cavity leading to a reduced bright pupil response. This effect is independent from external illumination. A possible solution is to use a parabolic mirror function for the IR HOE which follows the curvature of the eye.

6 CONCLUSION

In this work, we present a novel scanned LFI eye-tracking sensor approach, which is able to track the pupil with high robustness. Compared to VOG sensors and other scanned laser approaches, we highlight the outstanding robustness to ambient light and the high integrateability of our sensor approach into retinal projection AR glasses. We introduced the sensing technology, derived the physical foundations to describe the signal occurrence and propose a pupil extraction algorithm, which is optimized for the bright pupil signal characteristics measured by our sensor approach. To validate the accuracy of our scanned laser eye-tracking sensor we build a prototype using a modified retinal projection AR glasses setup based on the BML500P, a retinal projection system.

Our eye-tracking sensor achieves a mean accuracy of 1.674°, which is comparable to scanning laser eye-tracking approaches e.g. by [17]. We further solve typical problems of VOG eye-tracking sensors, e.g. the highly off axis integration of camera sensors by using an IR HOE to virtually place the laser scanner in front of the participants eye.

With the advancements especially in ambient light robustness and by the nearly invisible integration of the eye-tracking sensor we pave the way for eye-tracking sensors to become standard sensors for upcoming AR glasses, which will enable new application areas of eye-tracking e.g. long-term gaze monitoring for early detection of mental disorders.

ACKNOWLEDGEMENTS

Enkelejda Kasneci is a member of the Machine Learning Cluster of Excellence, EXC number 2064/1 - Project number 390727645.

REFERENCES

[1] 2014. IEC 60825-1:2014 Safety of laser products - Part 1: Equipment classification and requirements.

[2] Aayush K Chaudhary, Rakshit Kothari, Manoj Acharya, Shusil Dangi, Nitinraj Nair, Reynold Bailey, Christopher Kanan, Gabriel Diaz, and Jeff B Pelz. 2019. RITnet: Real-time semantic segmentation of the eye for gaze tracking. In *2019 IEEE/CVF International Conference on Computer Vision Workshop (ICCVW)*. IEEE, 3698–3702.

[3] Larry A. Coldren, Scott W. Corzine, and Milan L. Mashanovitch. 2012. *Diode Lasers and Photonic Integrated Circuits -*. John Wiley & Sons, New York.

[4] William A. Donnelly. 2008. The Advanced Human Eye Model (AHEM): a personal binocular eye modeling system inclusive of refraction, diffraction, and scatter. *Journal of refractive surgery* 24 9 (2008), 976–83. http://citeseerx.ist.psu.edu/viewdoc/download?doi=10.1.1.518.4567&rep=rep1&type=pdf

[5] Andrew T. Duchowski. 2018. Gaze-based interaction: A 30 year retrospective. *Computers & Graphics* 73 (2018), 59 – 69. https://doi.org/10.1016/j.cag.2018.04.002

[6] Wolfgang Fuhl. 2021. 1000 Pupil Segmentations in a Second using Haar Like Features and Statistical Learning. *arXiv preprint arXiv:2102.01921* (2021).

[7] Wolfgang Fuhl, Hong Gao, and Enkelejda Kasneci. 2020. Tiny convolution, decision tree, and binary neuronal networks for robust and real time pupil outline estimation. In *ACM Symposium on Eye Tracking Research and Applications*. 1–5.

[8] Wolfgang Fuhl, David Geisler, Thiago Santini, Tobias Appel, Wolfgang Rosenstiel, and Enkelejda Kasneci. 2018. CBF: Circular Binary Features for Robust and Real-time Pupil Center Detection. In *Proceedings of the 2018 ACM Symposium on Eye Tracking Research & Applications (ETRA 18)*. ACM, New York, NY, USA, Article 8, 6 pages. https://doi.org/10.1145/3204493.3204559

[9] Wolfgang Fuhl, Dennis Hospach, Thomas C. KÃijbler, Wolfgang Rosenstiel, Oliver Bringmann, and Enkelejda Kasneci. 2017. Ways of improving the precision of eye tracking data: Controlling the influence of dirt and dust on pupil detection. *Journal of Eye Movement Research* 10, 3 (May 2017). https://doi.org/10.16910/jemr.10.3.1

[10] Wolfgang Fuhl, Thiago Santini, Gjergji Kasneci, Wolfgang Rosenstiel, and Enkelejda Kasneci. 2017. Pupilnet v2. 0: Convolutional neural networks for cpu based real time robust pupil detection. *arXiv preprint arXiv:1711.00112* (2017).

[11] Wolfgang Fuhl, Thiago C Santini, Thomas Kübler, and Enkelejda Kasneci. 2016. Else: Ellipse selection for robust pupil detection in real-world environments. In *Proceedings of the Ninth Biennial ACM Symposium on Eye Tracking Research & Applications*. 123–130.

[12] Wolfgang Fuhl, Marc Tonsen, Andreas Bulling, and Enkelejda Kasneci. 2016. Pupil detection for head-mounted eye tracking in the wild: an evaluation of the state of the art. *Machine Vision and Applications* 27, 8 (01 Nov 2016), 1275–1288. https://doi.org/10.1007/s00138-016-0776-4

[13] Joseph W. Goodman. 2020. *Speckle Phenomena in Optics - Theory and Applications*. SPIE Press, Bellingham, Washington.

[14] Martin Grabherr, Philipp Gerlach, Roger King, and Roland Jäger. 2009. Integrated photodiodes complement the VCSEL platform. In *Vertical-Cavity Surface-Emitting Lasers XIII*, Vol. 7229. International Society for Optics and Photonics, 72290E.

[15] Boris Greenberg. 2021. EyeWay Vision: Highly Efficient Immersive AR Glasses Using Gaze-locked Exit Pupil Steering. In *SPIE AVR21 Industry Talks II*, Conference Chair (Ed.), Vol. 11764. International Society for Optics and Photonics, SPIE. https://doi.org/10.1117/12.2598227

[16] E.D. Guestrin and M. Eizenman. 2006. General theory of remote gaze estimation using the pupil center and corneal reflections. *IEEE Transactions on Biomedical Engineering* 53, 6 (2006), 1124–1133. https://doi.org/10.1109/TBME.2005.863952

[17] Kenneth Holmqvist, Saga Lee Orbom, Michael Miller, Albert Kashchenevsky, Mark M. Shovman, and Mark W. Greenlee. 2020. Validation of a Prototype Hybrid Eye-Tracker against the DPI and the Tobii Spectrum. In *ACM Symposium on Eye Tracking Research and Applications (ETRA 20 Full Papers)*. Association for Computing Machinery, New York, NY, USA, Article 6, 9 pages. https://doi.org/10.1145/3379155.3391330

[18] Anton S. Kaplanyan, Anton Sochenov, Thomas Leimkühler, Mikhail Okunev, Todd Goodall, and Gizem Rufo. 2019. DeepFovea: Neural Reconstruction for Foveated Rendering and Video Compression Using Learned Statistics of Natural Videos. *ACM Trans. Graph.* 38, 6, Article 212 (Nov. 2019), 13 pages. https://doi.org/10.1145/3355089.3356557

[19] Enkelejda Kasneci, Katrin Sippel, Kathrin Aehling, Martin Heister, Wolfgang Rosenstiel, Ulrich Schiefer, and Elena Papageorgiou. 2014. Driving with Binocular Visual Field Loss? A Study on a Supervised On-Road Parcours with Simultaneous Eye and Head Tracking. *PLOS ONE* 9, 2 (02 2014), 1–13. https://doi.org/10.1371/journal.pone.0087470

[20] Moritz Kassner, William Patera, and Andreas Bulling. 2014. Pupil: An Open Source Platform for Pervasive Eye Tracking and Mobile Gaze-based Interaction. In *Proceedings of the 2014 ACM International Joint Conference on Pervasive and Ubiquitous Computing: Adjunct Publication (UbiComp '14 Adjunct)*. ACM, New York, NY, USA, 1151–1160. https://doi.org/10.1145/2638728.2641695

[21] Jonghyun Kim, Youngmo Jeong, Michael Stengel, Kaan Akşit, Rachel Albert, Ben Boudaoud, Trey Greer, Joohwan Kim, Ward Lopes, Zander Majercik, Peter Shirley, Josef Spjut, Morgan McGuire, and David Luebke. 2019. Foveated

AR: Dynamically-foveated Augmented Reality Display. *ACM Trans. Graph.* 38, 4, Article 99 (July 2019), 15 pages. https://doi.org/10.1145/3306346.3322987

[22] Xiaoxu Meng, Ruofei Du, and Amitabh Varshney. 2020. Eye-dominance-guided Foveated Rendering. *IEEE Transactions on Visualization and Computer Graphics* 26, 5 (2020), 1972–1980. https://doi.org/10.1109/TVCG.2020.2973442

[23] Johannes Meyer, Adrian Frank, Thomas Schlebusch, and Enkeljeda Kasneci. 2022. A CNN-Based Human Activity Recognition System Combining a Laser Feedback Interferometry Eye Movement Sensor and an IMU for Context-Aware Smart Glasses. *Proc. ACM Interact. Mob. Wearable Ubiquitous Technol.* 5, 4, Article 172 (dec 2022), 24 pages. https://doi.org/10.1145/3494998

[24] Johannes Meyer, Thomas Schlebusch, Wolfgang Fuhl, and Enkelejda Kasneci. 2020. A Novel Camera-Free Eye Tracking Sensor for Augmented Reality based on Laser Scanning. *IEEE Sensors Journal* (2020), 1–9.

[25] Johannes Meyer, Thomas Schlebusch, Hans Spruit, Jochen Hellmig, and Enkelejda Kasneci. 2020. A Novel -Eye-Tracking Sensor for AR Glasses Based on Laser Self-Mixing Showing Exceptional Robustness Against Illumination. In *ACM Symposium on Eye Tracking Research and Applications (ETRA 20 Short Papers)*. Association for Computing Machinery, New York, NY, USA, Article 31, 5 pages. https://doi.org/10.1145/3379156.3391352

[26] Johannes Meyer, Thomas Schlebusch, Hans Spruit, Jochen Hellmig, and Enkelejda Kasneci. 2021. A compact low-power gaze gesture sensor based on laser feedback interferometry for smart glasses. In *Proc. of SPIE Vol*, Vol. 11788. 117880D–1.

[27] Johannes Meyer, Thomas Schlebusch, Hans Spruit, Jochen Hellmig, and Enkelejda Kasneci. 2021. A Novel Gaze Gesture Sensor for Smart Glasses Based on Laser Self-Mixing. In *CHI Conference on Human Factors in Computing Systems Extended Abstracts (CHI '21 Extended Abstracts)*. ACM, ACM, New York, NY, USA. https://doi.org/10.1145/3411763.3451621

[28] Rainer Michalzik. 2013. *VCSELs - Fundamentals, Technology and Applications of Vertical-Cavity Surface-Emitting Lasers*. Springer Berlin Heidelberg. https://doi.org/10.1007/978-3-642-24986-0

[29] AdHawk microsystems. 2021. *Ad-Hawk MindLink Specifications Preliminary Data Sheet*.

[30] Fabricio Batista Narcizo, Fernando EustÃąquio Dantas dos Santos, and Dan Witzner Hansen. 2021. High-Accuracy Gaze Estimation for Interpolation-Based Eye-Tracking Methods. *Vision* 5, 3 (2021). https://doi.org/10.3390/vision5030041

[31] Karlene Nguyen, Cindy Wagner, David Koons, and Myron Flickner. 2002. Differences in the Infrared Bright Pupil Response of Human Eyes. In *Proceedings of the 2002 Symposium on Eye Tracking Research & Applications (ETRA 02)*. Association for Computing Machinery, New York, NY, USA, 6. https://doi.org/10.1145/507072.507099

[32] Diederick C Niehorster, Thiago Santini, Roy S Hessels, Ignace TC Hooge, Enkelejda Kasneci, and Marcus Nyström. 2020. The impact of slippage on the data quality of head-worn eye trackers. *Behavior Research Methods* 52, 3 (2020), 1140–1160.

[33] Bernardo R. Pires, Myung Hwangbo, Michael Devyver, and Takeo Kanade. 2013. Visible-Spectrum Gaze Tracking for Sports. In *2013 IEEE Conference on Computer Vision and Pattern Recognition Workshops*. 1005–1010. https://doi.org/10.1109/CVPRW.2013.146

[34] Thiago Santini, Wolfgang Fuhl, and Enkelejda Kasneci. 2018. PuRe: Robust pupil detection for real-time pervasive eye tracking. *Computer Vision and Image Understanding* 170 (2018), 40–50.

[35] Thiago Santini, Wolfgang Fuhl, and Enkelejda Kasneci. 2018. PuReST: Robust pupil tracking for real-time pervasive eye tracking. In *Proceedings of the 2018 ACM symposium on eye tracking research & applications*. 1–5.

[36] Thiago Santini, Diederick C. Niehorster, and Enkelejda Kasneci. 2019. Get a Grip: Slippage-Robust and Glint-Free Gaze Estimation for Real-Time Pervasive Head-Mounted Eye Tracking. In *Proceedings of the 11th ACM Symposium on Eye Tracking Research & Applications (ETRA 19)*. Association for Computing Machinery, New York, NY, USA, Article 17, 10 pages. https://doi.org/10.1145/3314111.3319835

[37] N. Sarkar, B. O'Hanlon, A. Rohani, D. Strathearn, G. Lee, M. Olfat, and R. R. Mansour. 2017. A resonant eye-tracking microsystem for velocity estimation of saccades and foveated rendering. In *2017 IEEE 30th International Conference on Micro Electro Mechanical Systems (MEMS)*. 304–307. https://doi.org/10.1109/MEMSYS.2017.7863402

[38] N. Sarkar, D. Strathearn, G. Lee, M. Olfat, A. Rohani, and R. R. Mansour. 2015. A large angle, low voltage, small footprint micromirror for eye tracking and near-eye display applications. In *2015 Transducers - 2015 18th International Conference on Solid-State Sensors, Actuators and Microsystems (TRANSDUCERS)*. 855–858. https://doi.org/10.1109/TRANSDUCERS.2015.7181058

[39] Joseph M. Schmitt, S. H. Xiang, and Kin Man Yung. 1999. Speckle in optical coherence tomography. *Journal of Biomedical Optics* 4, 1 (1999), 95 – 105. https://doi.org/10.1117/1.429925

[40] Bosch Sensortec. 2020. *Smartglasses Light Drive*.

[41] Lech Swirski, Andreas Bulling, and Neil Dodgson. 2012. Robust Real-Time Pupil Tracking in Highly off-Axis Images. In *Proceedings of the Symposium on Eye Tracking Research and Applications (ETRA 12)*. Association for Computing Machinery, New York, NY, USA, 4. https://doi.org/10.1145/2168556.2168585

[42] Lech Świrski and Neil A. Dodgson. 2013. A fully-automatic, temporal approach to single camera, glint-free 3D eye model fitting [Abstract]. In *Proceedings of ECEM 2013*. http://www.cl.cam.ac.uk/research/rainbow/projects/eyemodelfit/

[43] Thomas Taimre, Milan Nikolić, Karl Bertling, Yah Leng Lim, Thierry Bosch, and Aleksandar D. Rakić. 2015. Laser feedback interferometry: a tutorial on the self-mixing effect for coherent sensing. *Adv. Opt. Photon.* 7, 3 (Sep 2015), 570–631. https://doi.org/10.1364/AOP.7.000570

[44] Tobii. 2021. *Pro Glasses 3 Product Description.* https://www.tobiipro.com/siteassets/tobii-pro/product-descriptions/product-description-tobii-pro-glasses-3.pdf/?v=1.4

[45] Marc Tonsen, Chris Kay Baumann, and Kai Dierkes. 2020. A High-Level Description and Performance Evaluation of Pupil Invisible. *arXiv preprint arXiv:2009.00508* (2020).

[46] Marc Tonsen, Julian Steil, Yusuke Sugano, and Andreas Bulling. 2017. InvisibleEye: Mobile Eye Tracking Using Multiple Low-Resolution Cameras and Learning-Based Gaze Estimation. *Proc. ACM Interact. Mob. Wearable Ubiquitous Technol.* 1, 3, Article 106 (Sept. 2017), 21 pages. https://doi.org/10.1145/3130971

[47] Tobias Wilm, Simone HÃűckh, Reinhold Fiess, and Wilhelm Stork. 2021. Holographic combiners for augmented reality applications fabricated by wave front recording. In *Novel Optical Systems, Methods, and Applications XXIV*, Cornelius F. Hahlweg and Joseph R. Mulley (Eds.), Vol. 11815. International Society for Optics and Photonics, SPIE, 13 – 22. https://doi.org/10.1117/12.2596838

[48] Yuk-Hoi Yiu, Moustafa Aboulatta, Theresa Raiser, Leoni Ophey, Virginia L. Flanagin, Peter zu Eulenburg, and Seyed-Ahmad Ahmadi. 2019. DeepVOG: Open-source pupil segmentation and gaze estimation in neuroscience using deep learning. *Journal of Neuroscience Methods* 324 (2019), 108307. https://doi.org/10.1016/j.jneumeth.2019.05.016

[49] Jianbo Zhao, Benjamin D. Chrysler, and Raymond K. Kostuk. 2021. Design of a waveguide eye-tracking system operating in near-infrared with holographic optical elements. *Optical Engineering* 60, 8 (2021). https://doi.org/10.1117/1.OE.60.8.085101

Received November 2021; revised January 2022; accepted April 2022